On the Latitude Variation of Ammonia, Acetylene, and Phosphine Altitude Profiles on Jupiter from HST Faint Object Spectrograph Observations

S. G. Edgington and S. K. Atreya

Department of Atmospheric, Oceanic, and Space Sciences, University of Michigan, Ann Arbor, Michigan 48109-2143
E-mail: Sgest@engin.umich.edu

L. M. Trafton

McDonald Observatory, University of Texas, Austin, Texas 78712

J. J. Caldwell

Department of Physics and Astronomy, York University, North York, Ontario M35 1P3, Canada

R. F. Beebe and A. A. Simon

Astronomy Department, New Mexico State University, Las Cruces, New Mexico 88033

R. A. West

Jet Propulsion Laboratory, California Institute of Technology, 4800 Oak Grove Drive, Pasadena, California 91109

and

C. Barnet

NASA Goddard Space Flight Center Greenbelt, Maryland 20771

Ultraviolet spectra in the spectral region from 160 to 230 nm were taken with the Hubble Space Telescope Faint Object Spectrograph in May 1992. We analyze these data to obtain the altitude distribution of ammonia and its variation with latitude from 6°N to 25°N. Ammonia condenses below the 150-mbar level, above which it departs from saturation due to photolysis. Using a photochemical model, we also derive the value of atmospheric eddy mixing coefficients at the observed latitudes. It is found that the eddy diffusion coefficient varies from 1.5×10^4 cm^2 s^{-1} at 450 mbar to 4.9×10^2 cm^2 s^{-1} at 120 mbar. The vertical distribution of ammonia and the eddy diffusion coefficient do not show a large variation with latitude. We also determine an acetylene mixing ratio of $(10–30) \times 10^{-9}$ near 80 mbar and an upper limit of 1.5×10^{-7} for the phosphine mixing ratio, if PH$_3$ is mixed uniformly below the 140 mbar level. The existence of particulate haze at low and high latitudes is also investigated.   © 1998 Academic Press

INTRODUCTION

The spatial distribution of molecular species in Jupiter's atmosphere is important for the understanding of jovian aeronomy, dynamics, and circulation. From spectral observations of the composition and abundance, information such as the vertical mixing and important chemical processes can be inferred. Evidence for horizontal and vertical inhomogeneities in the jovian atmosphere is readily seen in the color variations and banded appearance observed in images of the jovian cloud features (Fig. 1). These cloud features and their spatial structure exist in the troposphere at pressures of approximately 0.5 bars and greater. It is reasonable to ask how the atmosphere of Jupiter in the upper troposphere and lower stratosphere varies spatially and how this might be reflected in the observed altitude distribution of various constituents. Remote sensing in the ultraviolet from 160 to 340 nm provides a means of de-
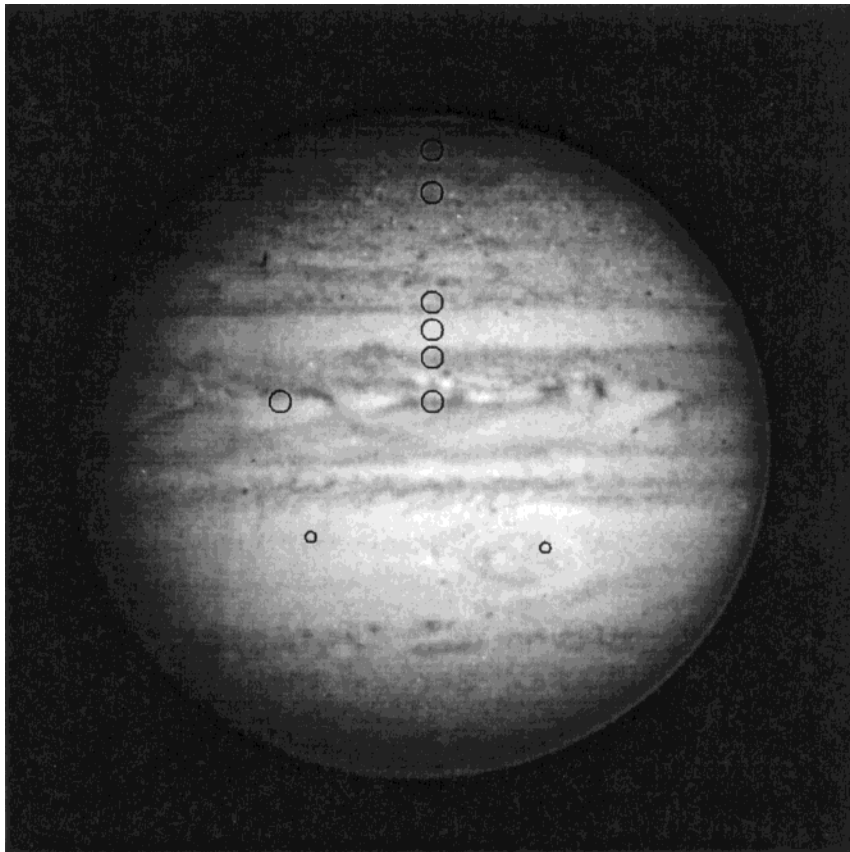
FIG. 1. Image of Jupiter taken with WF/PC at 718 nm. The black circles correspond to observations taken at 6°N, 15°N, 20°N, 25°N, 48°N, and 65°N along the central meridian during the Cycle 1 campaign, with the exception of the GRS, SEB, and equatorial plume, where they correspond to the actual longitudes observed. The size of the black circles corresponds to the FOS aperture projected on the planet.

termining such information for constituents like ammonia, acetylene, phosphine, and aerosol particles. Mixing ratios of these constituents at various altitudes can be obtained by inverting the data on the absorption and reflection of the UV solar photons.

Observations related to the aforementioned molecules in Jupiter's atmosphere have been performed with spectrometers on sounding rockets (Giles *et al.* 1976; Clarke *et al.* 1982), the International Ultraviolet Explorer (IUE) (Combes *et al.* 1981; Wagener *et al.* 1985), Voyager UV Spectrometer and Infrared Interferometer Spectrometer (IRIS) instruments (Festou *et al.* 1981; Kunde *et al.* 1982; Carlson *et al.* 1994), and ground-based infrared, radio, and microwave techniques, including the Very Large Array (dePater and Massie 1985) and the Caltech Submillimeter Observatory (Weisstein and Serabyn, 1994). These measurements have led to a determination of the distributions of ammonia, acetylene, and phosphine in the stratosphere and troposphere of Jupiter and, to a lesser extent, their variation with latitude.

Radio observations yield larger than solar mixing ratios of NH_3 (solar N/H $= 1.12 \times 10^{-4}$; Anders and Grevesse

1989) with values of $(2.2–3) \times 10^{-4}$ in the deep, mixed atmosphere (dePater and Massie 1985). The NH_3 volume mixing ratios measured by IRIS near 1 bar have been shown to vary between 1.5×10^{-4} and 3.0×10^{-4} depending upon whether belts or zones are observed (Kunde *et al.* 1982; Carlson *et al.* 1994). At 3 bar the mixing ratio falls in the range $(3.8–4.8) \times 10^{-4}$, dependent, once again, upon whether a belt or zone is being observed. In the 0.2–0.8 bar region, the abundance has been shown to decrease with altitude. Observations in the UV by Greenspan and Owen (1967), Tomasko (1974), and Combes *et al.* (1981) have shown that the abundance of ammonia in the upper troposphere/stratosphere is orders of magnitude lower than the abundance in the lower troposphere and lower than the abundance expected from the ammonia saturation vapor pressure in that region of the atmosphere. Combes *et al.* (1981) provided the first direct identification of NH_3 in the stratosphere by sampling the region of the atmosphere near 100 mbar with the IUE and also found it to be subsaturated. Several altitude profiles were attempted to obtain a fit to the IUE spectra, but due to the poor spectral resolution of the IUE, a unique result could not be obtained.

Acetylene has been measured at wavelengths of 160–180 nm by a number of observations including IUE (Wagener *et al.* 1985; Owen *et al.* 1980; Gladstone *et al.* 1983; McGrath *et al.* 1989) and the Hopkins Ultraviolet Telescope (HUT) during the Astro-1 and Astro-2 missions on board the Space Shuttle (Morrissey *et al.* 1995). These studies, which sample the region above the 80 mbar level, have yielded mixing ratios of $(30 \pm 10) \times 10^{-9}$, 22×10^{-9}, 100×10^{-9}, 35.5×10^{-9}, $39^{+4}_{-3} \times 10^{-9}$, $28^{+3}_{-2} \times 10^{-9}$, respectively. Acetylene has also been observed in the IR at ~ 13 μm yielding abundances of $(20–80) \times 10^{-9}$ in the stratosphere (Noll *et al.* 1986) which is consistent with Voyager IRIS measurements of $(30–100) \times 10^{-9}$ (Hanel *et al.* 1979). The IR data sample at lower pressures than the IUE and HUT measurements. Voyager UV stellar occultation measurements observed an upper limit of 5×10^{-6} at 10 μbar (Festou *et al.* 1981). This would indicate that the acetylene mixing ratio could increase with altitude as is expected on the basis of photochemical models (Strobel 1973; Atreya *et al.* 1981; Gladstone *et al.* 1996).

Phosphine, was first detected by Ridgway *et al.* (1976) in the IR at 10 μm. Several other measurements in the IR (Larson *et al.* 1977; Beer and Taylor 1979; and Encrenaz *et al.* 1978) have also detected phosphine. At these wavelengths, the atmosphere from pressures of 0.2 bars and greater is probed. Analysis of these spectra have yielded mixing ratios of $(0.9–1.8) \times 10^{-7}$ for <560 mbar and 5×10^{-7} for pressures greater than 600 mbar. Voyager IRIS observations (Kunde *et al.* 1982; Drossart *et al.* 1982) yield mixing ratios of $(1–2) \times 10^{-7}$ between 0.2 and 0.6 bar and 6×10^{-7} for pressures greater than 1 bar. Observations at submillimeter wavelengths (Weisstein and Serabyn 1994) only give an upper limit of 5×10^{-7} near 500 mbar. Phosphine has not been detected in the UV, although the distribution determined from the IRIS data set is consistent with the nondetection in IUE observations (Wagener *et al.* 1985).

Most of the previous observations are for the equatorial and polar regions yielding no latitude variation. The distribution of molecular species with altitude in most cases was not determined. However, the relatively high angular resolution of 1 arcsec obtainable from the Hubble Space Telescope Faint Object Spectrograph (HST/FOS) allows the sampling of the jovian disk at a number of latitudes, thus providing information about the latitudinal variation of the reflected UV flux and hence molecular species, aerosols, and dynamics over regions corresponding to several belts and zones, the Great Red Spot, and other cloud features.

The spectra of Jupiter observed in the near ultraviolet are due to the scattering of solar photons by the ambient atmosphere along with absorption by various molecules and aerosol particles. An analysis of the scattering and absorption characteristics of photons at different wave-lengths allows us not only to identify species present in the atmosphere, but also to probe different altitudes of the atmosphere since Rayleigh scattering cross sections vary with wavelength, to first order, as the inverse of the fourth power of the wavelength. Therefore, the pressure level where the Rayleigh scattering optical depth is unity moves higher in the atmosphere with decreasing wavelength since a smaller column of atmosphere is sufficient to cause the scattering. Absorption by gases and aerosol particles will modify the optical depth due to Rayleigh scattering. Sampling over a large wavelength interval in the ultraviolet allows determination of altitude profiles of UV absorbing material, provided that the molecular absorption takes place over a comparatively large enough portion of the wavelength interval.

During the period of May 19–25, 1992, the Faint Object Spectrograph (FOS) on HST was used to observe Jupiter in the ultraviolet from 160–350 nm, obtaining spectra at several latitudes in the northern hemisphere. We report the results on the latitude variation and altitude distributions of NH_3, C_2H_2, and PH_3 in the upper troposphere and the lower stratosphere. We derive the values of vertical eddy diffusion coefficient from the altitude profiles of observed species and current photochemical models of the jovian atmosphere. Analysis is restricted to the measurements done in the 160–230 nm range, since all three molecules can be observed in this wavelength region. Spectra at wavelengths greater than 230 nm contain pronounced aerosol effects. The measurements made at longer wavelengths as well as the Great Red Spot, the South Equatorial Belt, and the June 6, 1993 observations of the southern hemisphere will be reported in a later paper.

OBSERVATIONS

The observations were done during Cycle 1 in 1992 using the Faint Object Spectrograph on the Hubble Space Telescope. We report observations taken with grating G190H with the $1''$ circular aperture to obtain spectra ranging from 160 nm to 230 nm at a resolution of 0.34 nm. The size of the aperture translates into a footprint of radius ~ 3900 km at Jupiter. Various regions of the planet were targeted, mostly in the northern hemisphere and equatorial zone. Study of the southern hemisphere was left for Cycle 2. In particular, we report the results from spectra taken along the central meridian longitude (CML) at planetographic latitudes corresponding to the following regions: a jet along the northern edge of the Equatorial Zone (6°N), the North Equatorial Belt to the south of a westward jet (15°N), the North Tropical Zone to the south of an eastward jet (20°N), the North Temperate Belt (25°N), eastward and westward jets at 48°N, and the auroral region (65°N). In addition, spectra were obtained of a potential equatorial plume near 6°N, the Great Red Spot, and the nearby South Equatorial

TABLE I
Observations

Date	Mean time (UT)	Exposure time (min)	Nominal latitude (°)	Approximate projection on surface (°)	CML (°; Sys III)
1992 May 25	10:17	24	EQ Plume	−1.5–1.5	140
1992 May 21	22:47	15	6°N CML	4.5–7.5	351
	23:57	15			34
1992 May 25	5:12	24	15°N CML	13.4–16.6	316
1992 May 26	6:56	24	20°N CML	18.4–21.6	162
1992 May 20	4:50	24	25°N CML	23.3–26.7	270
1992 May 22	5:07	15	48°N CML	45.7–50.3	222
	6:23	15			267
1992 May 22	12:53	15	65°N CML	61.2–68.8	143
	13:13	15			153

Belt. Figure 1 shows a Wide Field Planetary Camera (WF/PC) image of Jupiter taken during the same observational time period with the points of observation along the Central Meridian marked. The nominal latitudes and longitudes of the observations are summarized in Table I.

HST tracked Jupiter's orbital motion accurately, but Jupiter's rotation was not tracked. Due to the rotation, the longer (24-min) exposures can be smeared over as much as 14.4° of longitude . The resulting spectra not only represent an average over the projected size of the aperture, but also over a number of longitudes depending on the exposure time.

The modeling of the albedo is dependent on the actual position being targeted. This is especially important for the high-latitude spectra, where pointing errors can translate into large errors in the solar and Earth zenith angles. Blind pointing, which assumes that the position of the target is accurately known relative to guide stars used by HST, was used for all observations. This has an a priori one-sigma uncertainty comparable to the diameter of the 1″ aperture. However, the relative pointing has less error and the spatial offset could be derived by evaluating the pointing accuracy of HST WF/PC images taken in conjunction with this program. Future refinements for the targeting are expected with the use of the Moving Object Support System ephemeris software at the Space Telescope Science Institute (STScI).

DATA REDUCTION

The FOS observes the flux of radiation from Jupiter entering through a solid angle defined by the aperture size. These photons are focused onto an array of 516 diode channels which register photoelectron pulses. Each diode of the detector was oversampled using 4:1 substepping, which shifts the spectrum a quarter of a diode for each substep, producing an array of count rates of dimension 2064. The raw data were reprocessed to produce absolute intensities vs wavelength, since the pipeline reductions provided by STScI did not account for the extended nature of Jupiter in the absolute calibration nor for the grating scatter of visible light prominent below 200 nm. To account for this grating scatter, we made use of Jupiter's exponentially declining continuum intensity below 200 nm, which becomes undetectable below about 170 nm due to background noise from instrumental dark and grating scattered photons. We strongly smoothed each jovian G190H count rate spectrum over 200 channels and subtracted the asymptotic value at 160 nm before converting to flux. Too much subtraction would give a negative flux. The value subtracted was of order 1 Hz/channel for the larger aperture spectra and 0.1 Hz/channel for the smaller aperture spectra. This compares with maximum count rates for G190H varying between 6 and 700 Hz per channel. The underlying assumption is that the grating scatter is gray in count rates below 230 nm. Cunningham and Caldwell (1993) show that this is valid above 175 nm. To improve the S/N ratio, we then binned the spectra 2:1 to produce arrays of dimension 1032. This still permits a 2:1 oversampling per diode.

The flux calibration curves assumed a point source (star) and accounted for the light not entering the aperture owing to HST's aberrated point spread function. However, for a uniform extended source, there are no such net losses. We therefore corrected the derived fluxes for the wavelength-dependent aperture transmissions based on information provided by STScI.

The normal reflectivities (albedos) were calculated as

$$\frac{I}{F} = \frac{d^2 F_{\mathrm{J}}}{F \, \Delta\Omega},$$ (1)

where I is the intensity in photons cm^{-2} s^{-1} ster^{-1} nm^{-1}, πF is the solar flux measured at the Earth in photons cm^{-2}

s^{-1} nm^{-1}, F_J is Jupiter's flux as seen with the FOS corrected for an extended source, d is Jupiter's distance from the Sun in astronomical units (AU), and $\Delta\Omega$ is the solid angle of the aperture in steradians. Jupiter was located 5.42 AU from the Sun during the time of observation. To derive the normal reflectivities and to cancel out the diffusely reflected solar lines from the Jupiter spectra, we used the Solar Ultraviolet Spectral Irradiance Monitor (SUSIM) (Van Hoosier *et al.* 1988) solar spectrum taken on board the Space Shuttle to remove the solar lines. However, below about 230 nm, the solar spectrum varies noticeably over the solar cycle and it is desirable to use a solar spectrum taken under the same conditions of solar activity as during the HST Jupiter observations. For this purpose, we obtained a Solar–Stellar Irradiance Comparison Experiment (SOLSTICE) spectrum (G. Rottman, personal communication, 1993) taken on May 26, 1992 corrected to 1 AU. As expected the two solar spectra have different continuum variations. Since the SOLSTICE spectrum is only sampled every 1 nm, whereas the SUSIM spectrum is sampled every 0.01 nm, the SOLSTICE spectrum could not be used directly to determine the albedos. We corrected the Jupiter albedo spectra derived using the SUSIM solar spectrum by multiplying them by an "optimally smoothed" SUSIM/SOLSTICE normalization using the algorithm of Brault and White (1971). The resulting albedos (reflectivities) are shown in Fig. 2 for several latitudes.

To cancel the solar lines adequately, we approximated the FOS line spread function by a Gaussian with the full-width-at-half-max as a free parameter and convolved the solar spectra by this function. The photometrically accurate SUSIM spectrum suffers from a nonlinearity in the wavelength scale. Allowing therefore for a wavelength shift and scale error relative to the Jupiter spectra, we let the wavelength shift and scale also be free parameters and performed a root-mean-square fit of each Jupiter spectrum to the convolved solar SUSIM spectrum, varying all three parameters to produce the maximum agreement. This procedure also yielded the jovian wavelengths in the reference frame of the solar spectrum. The agreement is not perfect, however, in that strong solar lines yield apparent absorption features detectable in the spectra, e.g., near 225 nm. We attribute these to Raman scattering in Jupiter's atmosphere and incomplete knowledge of the point spread function. Use of this procedure for Uranus and Neptune, where Raman scattering is stronger, should be cautioned as the stronger Raman features could cause misalignment of the spectra.

The absolute calibration is good to 8–10% not including the uncertainty due to grating scatter. The statistical errors were recomputed and propagated throughout the reductions including combining spectra, binning, smoothing, and division by the solar spectrum. Owing to the

exponentially declining signal from Jupiter for wavelengths below 200 nm, the derived albedo becomes progressively uncertain owing to its increasing dependence on the error in removing the grating scattered light contribution. This uncertainty in the background counts is reflected in the divergence of the propagated statistical error of the normal reflectivities at wavelengths shorter than 170 nm (Fig. 2). A small increase in the grating scatter correction translates into a progressively bigger adjustment of Jupiter's continuum spectrum below about 180 nm. Below this wavelength, Jupiter's continuum is uncertain and cannot be reliably derived from the observations. However, this spectral region contains information in the form of equivalent width of absorption lines relative to the continuum, which is not affected by the uncertainty in the absolute continuum level. We therefore include wavelengths and intensities down to 175 nm in our plots and analysis.

METHOD OF ANALYSIS

The goal of our analysis of the FOS observations is one of identifying possible absorbing, emitting, and scattering species and determining their altitude distributions. Ultimately, the source of the observed UV light coming from Jupiter is the Sun. Photons are Rayleigh–Raman scattered by the ambient hydrogen, helium, and methane atmosphere at these wavelengths. The Rayleigh scattering cross section for H_2 using the parameterization given by Ford and Browne (1973) for a gas at 100°K with an *ortho-para* ratio of 3:1 is given by

$$\sigma_{H_2}^{Rayleigh} = \left(\frac{10^8}{\lambda}\right)^4 \left(8.34 \times 10^{-45} \right.$$
$$+ \frac{1.25 \times 10^{-38}}{\lambda^2} + \frac{1.53 \times 10^{-32}}{\lambda^4} \qquad (2)$$
$$\left. + \frac{1.74 \times 10^{-26}}{\lambda^6} + \frac{1.94 \times 10^{-20}}{\lambda^8} \right),$$

where λ is in Angstroms and $\sigma_{H_2}^{Rayleigh}$ is in cm^{-2}. The H_2 *ortho/para* ratio of 3:1 is the thermodynamic equilibrium value. Although the ratio differs from the value in the jovian troposphere (Conrath and Gierasch, 1983), deviations from this value lead to changes of less than 1% in the Rayleigh cross section. The Rayleigh scattering cross section for He was calculated using the parameterization for the index of refraction given by Allen (1973) after finding good agreement with the experimental data of Smith *et al.* (1976). The resulting expression for the He Rayleigh scattering cross section is given by
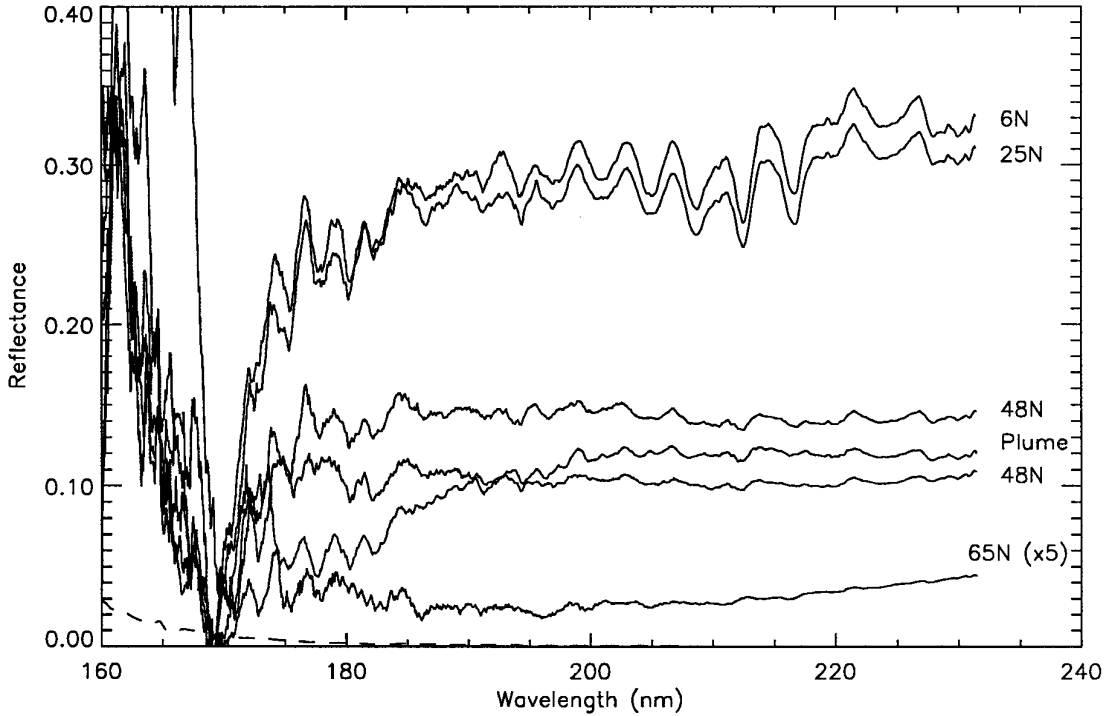
FIG. 2. Normal reflectance (I/F) at several latitudes considered in our analysis. Spectra for 15°N and 20°N (both not shown) lie between those of 6°N and 25°N with a decreasing albedo with increasing latitude. The observation of the plume took place near the limb (~80° from CML) resulting in a low albedo compared to the CML observations. The propagated statistical error for 6°N is shown by the dashed curve. Below 180 nm, grating scattered photons dominate the albedo.

$$\sigma_{He}^{Rayleigh} = \left(\frac{10^8}{\lambda}\right)^4 \left(5.78 \times 10^{-46} + \frac{2.66 \times 10^{-40}}{\lambda^2}\right.$$
$$\left. + \frac{3.06 \times 10^{-35}}{\lambda^4}\right). \tag{3}$$

The helium-to-hydrogen ratio was taken to be the value 0.157 obtained by both the Galileo probe mass spectrometer (Niemann *et al.*, 1996) and the He abundance detector (von Zahn and Hunten, 1996). Methane, the next most abundant constituent in the jovian atmosphere, was included for completeness, even though its abundance is approximately a factor of one thousand smaller than that of hydrogen. We use the index of refraction given in Allen (1973) in calculating the methane Rayleigh scattering cross section.

Raman scattering shifts a photon from its original wavelength by an amount corresponding to the energy needed to excite various rotational and vibrational states of H_2. It has been neglected in the analysis of these spectra, because this scattering is weak compared to absorption by the molecules at wavelengths of interest. Rotational Raman scattering features are evident in Jupiter's UV albedo spectra at longer wavelengths (>225 nm) taken with the G270H

grating. Strong solar lines are not fully canceled owing to the partial filling in of the cores of the diffusely reflected solar lines in Jupiter's spectrum; they appear as weak emission features at the wavelengths of the strong solar lines. To first order, however, the total number of emergent photons is conserved in rotational Raman scattering, assuming the continuum is flat; therefore, the emergent flux is not affected when averaged over a band wide enough to include both the incident photons and rotational Raman scattered photons. Vibrational scattering, on the other hand, causes a shift out of the passband and results in an effective absorption. These photons will be lost in the increasing solar flux and hence contribute little to the continuum. In the continuum region, where gas absorption is weak, approximately 0.5–2.0% of photons will actually undergo Raman scattering (Cochran and Trafton, 1978). Even a small amount of background gas absorption will greatly reduce the mean path length of emergent UV photons in Jupiter's atmosphere and hence greatly reduce the probability of Rayleigh and Raman scattering. We therefore expect Raman scattering to be negligible over Jupiter's gaseous absorption bands investigated here and assume that our fits of the synthetic spectra to the observations may safely neglect the effects of Raman scattering. Also

not treated in our analysis are the effects of spherical geometry, which is unimportant near the central meridian, and polarization of natural light.

A fraction of the solar photons are absorbed by the various chemical species depending on the strength of the photoabsorption cross section for the species relative to the Rayleigh scattering cross-section. The strength of this absorption can vary with wavelength depending upon the nature of the interaction of the photons with the molecule. At a particular wavelength, the majority of photons will originate from altitude levels (roughly where the total optical depth equals unity) determined by the absorption/scattering cross-sections. Thus, the altitude dependence can be determined from the presence of three effects: Rayleigh scattering of light, the absorption cross-sections of chemical species, and aerosol absorption and scattering. Light observed at these wavelengths results from the integrated contribution of each altitude level over the line of sight followed by averaging over the solid angle of the FOS aperture. Dividing this observed intensity by F, where πF is the solar flux at Jupiter, gives the albedo or reflectivity according to Eq. (1).

We model the observed albedo by solving the radiative transfer equation given by

$$
\mu \frac{d}{dz} \frac{I(z, \Omega)}{F} = - \sum_i n_i (\sigma_i^{abs} + \sigma_i^{scat}) \frac{I(z, \Omega)}{F} \\
+ \sum_i n_i \sigma_i^{scat} \oint p_i(z, \Omega, \Omega') \frac{I(z, \Omega')}{F} d\Omega'
$$
(4)

for a plane parallel atmosphere, where μ is the cosine of the zenith angle, Ω and Ω' are directional solid angles, n_i is the number density of species i (which includes both gases and aerosol), σ_i^{abs} and σ_i^{scat} are the absorption and scattering cross sections, and $p_i(z, \Omega, \Omega')$ is the scattering phase function. The altitude profile for mixing ratios can be obtained by solving the forward radiative transfer problem and iteratively adjusting the altitude profile of each species until the modeled reflectivities agree with the observed. This iteration was performed by adjusting the eddy mixing coefficient followed by self-consistently solving for the radiation field and mixing ratios using the photochemical model to be described later. Uncertainty in the cross sections and phase functions will likely lead to nonuniqueness in the derived mixing ratios.

Once the I/F reflectivities were obtained from the reduction of the FOS spectra described in the previous section and an altitude profile was obtained for each chemical species, a multiple scattering radiative transfer code DISORT (Stamnes et al. 1988) was used to generate our modeled reflectances at a resolution of 0.1 nm. This code solves the radiative transfer equation by the discrete ordinates method (Chandrasekhar, 1960) which breaks

up the light into an arbitrary number of directional streams in the zenith. Comparing fits using a different number of streams (≥ 2) showed that eight or more were satisfactory in modeling the albedo. Thus we chose to use eight in generating the synthetic spectra. After the FOS spectra and simulated I/F spectra were smoothed to the same resolution of 0.4 nm, which is the effective resolution of the FOS G190H grating, the two were compared to determine whether a good fit was obtained. Smoothing was performed using a weighted average as discussed by Young (1962),

$$
\langle y \rangle = \sum_i \frac{y_i}{\sigma_i^2} \bigg/ \sum_i \frac{1}{\sigma_i^2}
$$
(5)

where y_i and σ_i are the reflectivity and propagated statistical error, respectively, and i represents the number of wavelength bins summed over. Inputs to the radiative transfer code were the photoabsorption cross sections of the molecular species considered, the number density (mixing ratio) of each species vs. altitude, the solar zenith angle, the Earth zenith angle, the azimuth angle between the Earth and the Sun, and the model atmosphere (here defined as temperature and pressure vs altitude). Table II lists the zenith and azimuth angles at each latitude used in these calculations. The temperature vs pressure profiles were taken to be those obtained by the Voyager II UVS, IRIS, and radio science measurements (Festou et al. 1981; Hanel et al. 1979; Lindal et al. 1981), which are comparable to the derived Galileo temperature–pressure profile (Seiff et al. 1996) below the 1 mbar pressure level. Above this level, the temperature departs from that inferred from Voyager data. This departure has a negligible effect on the mixing ratios in the lower stratosphere/upper troposphere and is important only above the methane homopause where the scale height is increased.

To assist in the analysis and interpretation of the FOS spectra, photochemical models of the ammonia (Atreya et al. 1977), hydrocarbon (Atreya and Romani 1985, Gladstone et al. 1996, Bishop et al. 1997), and phosphine chemistry (Strobel 1977, Kaye and Strobel 1984) were used to generate the altitude profiles of the absorbing species seen in our wavelength interval. In this analysis, all of the above chemistries are treated in a single model. This model solves the steady state diurnal averaged one dimensional coupled continuity–diffusion equation for each species i, given by

$$
\frac{\partial}{\partial z}(n_i w_i) = P_i - L_i
$$
(6)

and

TABLE II
Relevant Earth/Sun Angles

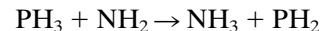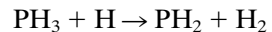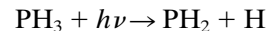| Latitude (°)	Solar zenith (°)	Earth zenith (°)	Azimuth (°)	Average solar zenith (°)	Fraction of day
6 N	13.3	7.29	54.6	50.9	0.499
15 N	19.8	16.3	33.4	52.4	0.497
20 N	24.2	21.3	27.1	53.7	0.496
25 N	28.7	26.3	22.9	55.3	0.495
48 N	50.6	49.3	13.98	65.6	0.489
65 N	67.2	66.3	11.7	75.4	0.479
Plume	80.18	69.5	0.00298	50.9	0.499

$$n_i w_i = -D_i n_i \left(\frac{1}{n_i} \frac{\partial}{\partial z} n_i + \frac{(1 + \alpha_i)}{T_i} \frac{\partial}{\partial z} T_i + \frac{m_i g}{k T_i} \right)$$

$$- K_i n_T \frac{\partial}{\partial z} \left(\frac{n_i}{n_T} \right) \tag{7}$$

where P_i designates the production, L_i is the loss, n_i is the number density, D_i is the molecular diffusion coefficient, α_i is the thermal diffusivity, K_i is the eddy diffusivity, w_i is the vertical velocity, T_i is the temperature, all for species i, g is gravity, and n_T is the total number density. Diurnal averaging was performed as detailed in Romani and Atreya (1988) and is discussed in the Appendix. Details about the specific chemistry considered in each model are given in Atreya *et al.* (1977), Bishop *et al.* (1997), and Kaye and Strobel (1984).

Major improvements to these models include updated reaction rates for several chemical reactions, an improved multiple scattering radiative transfer algorithm, and coupling of the major photochemical families through competing reactions with atomic hydrogen and competing absorption of solar ultraviolet photons. The quantum yields of the products of methane photolysis have been updated to those used by Romani (1996) (CH_3: 0.41, $^3CH_2$: 0.21, $^1CH_2$: 0.28 CH: 0.1), which account for experiments of Mordaunt *et al.* (1993). Note, however that the new quantum yields, which give $CH_3 + H$ as a major pathway, have a negligible effect on the earlier hydrocarbon chemistry. The original quantum yields ($^3CH_2$: 0.51, $^1CH_2$: 0.41, CH: 0.08) lead to the formation of $^1CH_2$, which is quickly converted to CH_3 through subsequent chemistry. We use the rate constants of Fahr *et al.* (1995) for the reaction of $H_2 + C_2H_3 \rightarrow C_2H_4 + H$ ($k = 5.0 \times 10^{-20} \, T^{2.63} \exp(-4298/T)$ cm^3 s^{-1}; $\geq 10^{-23}$ cm^3 s^{-1}) and of Fahr *et al.* (1991) and Monks *et al.* (1995) for the reactions $H + C_2H_3 \rightarrow C_2H_2 + H_2$ ($k_0 = 1.49 \times 10^{-27}$ cm^6 s^{-1}; $k_\infty = 1.55 \times 10^{-10}$ cm^3 s^{-1}) and $H + C_2H_3 + M \rightarrow C_2H_4 + M$ ($k = 5.0 \times 10^{-11}$ cm^3 s^{-1}). A detailed analysis of the inclusion of these reactions has been published by Romani (1996). These rate constants have a negligible impact on the stratospheric mixing ratio

of ethane, whereas large effects are seen for the mixing ratio of acetylene. The rate constant of Khe *et al.* (1977) for $NH_2 + NH_2 + M \rightarrow N_2H_4 + M$ ($k = 2.49 \times 10^{-11}$ cm^3 s^{-1}) was also chosen. This differs from the rate ($k = 1.0 \times 10^{-10}$ cm^3 s^{-1}) used in the earlier studies of Atreya *et al.* (1977) and Strobel (1973) and results in an increase in the ammonia mixing ratio in the stratosphere as more amidogen (NH_2) radicals are permitted to react with atomic hydrogen to recycle ammonia.

The chemistry resulting from the photolysis of phosphine has been included in several photochemical models of Jupiter, e.g. Strobel (1977), but has been studied in detail only for the case of Saturn (Kaye and Strobel, 1984). Many of the reaction rates involving phosphorus compounds are unknown and were approximated by various methods in the above models. We have modeled the phosphine photochemistry using a simple reaction mechanism given by

$$PH_3 + h\nu \rightarrow PH_2 + H$$

$$PH_2 + H \rightarrow PH_3$$

$$PH_3 + H \rightarrow PH_2 + H_2$$

$$PH_3 + NH_2 \rightarrow NH_3 + PH_2$$

$$PH_2 + PH_2 \rightarrow P_2H_4$$

$$\rightarrow PH + PH_3$$
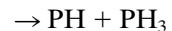
with rates taken from Kaye and Strobel (1984). In the above photochemical scheme, P_2H_4 is expected to condense out and PH (the minor pathway of the two) will eventually lead to the formation of P_2 and other forms of elemental phosphorus, e.g., P_4. Hence, both P_2H_4 and PH contribute little to the recycling of phosphine. Coupling in the form of CH_3PH_2 is excluded since the reaction of CH_3 with PH_2 is expected to have little impact on the abundance of PH_2 and hence PH_3. Given the lack of experimental data on reaction rates and thermal properties of phosphorus-bearing species, the above chemical scheme represents our best current estimate of the nature of phosphine photo-

chemistry in Jupiter's atmosphere. On the other hand, some constraints on PH_3 may be obtained from the FOS data discussed in this paper.

The photochemical model was also modified to include a delta-two-stream approximation (Wiscombe, 1977) similar to the one used in Atreya *et al.* (1995) to model the radiation field, whereas previous photochemical models used a Beer's law approximation. This modification has the physical effect of increasing photolysis rates (Visconti 1981; Kaminski and McConnell 1991) in regions where the atmosphere becomes optically thick to scattering. It is most important in modeling the nitrogen, hydrocarbon, and phosphorus chemistry at low altitudes, especially in altitude regions containing aerosol particles and in wavelength regions where photons are absorbed by a number of spectrally active species. This modification also allows us to estimate the albedo at low resolution (1 nm) before using the more computationally challenging higher resolution (0.1 nm) multistream radiative transfer code discussed above.

For each latitude that was observed, the remaining free parameters left in our photochemical model are the aerosol radiative properties and the eddy diffusion coefficient. In this paper, aerosol is used to refer to any condensed material. As the aerosol composition in the jovian atmosphere is unknown and ultraviolet optical constants for a number of possible candidates have yet to be measured in the lab, aerosols were treated simply by specifying a phase function and single scattering albedo at each wavelength, both determined using Mie scattering theory for an appropriate index of refraction and mean particle size, and the aerosol abundance for each altitude level.

In the upper atmosphere below the homopause, the eddy diffusion coefficient was taken to be of the form

$$K = K_0 \left(\frac{n}{n_0} \right)^{-0.6}, \tag{8}$$

where $k_0 = 1.4 \times 10^6$ cm^2 sec^{-1} and $n_0 = 1.4 \times 10^{13}$ cm^{-3} at the homopause as determined from Voyager ultraviolet solar occultation measurements (Atreya *et al.* 1981). This parameter is important in determining the profile of hydrocarbons, especially acetylene, in the atmosphere. In the lower atmosphere, where ammonia and phosphine are present, this parameterization could break down due to turbulent processes. Adjusting the eddy diffusion coefficient until the species altitude profiles best fit the observational data allows us to determine the variation of K with pressure in the lower stratosphere.

MODEL FITS AND THEIR INTERPRETATION

In our analysis of the FOS reflectances, we have included three molecules; ammonia, acetylene, and phosphine, along with hydrogen and helium, which Rayleigh scatter the incoming sunlight. The signature of the first two species is clearly present in most of the observations, as can be seen by comparing their unique UV absorption characteristics (Fig. 3) with the reflectances (Fig. 2). Phosphine has a continuum cross section and hence is difficult to distinguish from any species or aerosol with similar absorption properties. Low-temperature cross-sections of ammonia, acetylene, and phosphine were taken from Chen *et al.* (1991, 1995). The photoabsorption cross sections of important molecules considered in the analysis are shown in Fig. 3.

Several other molecules can be ruled out as spectral absorbers on the basis of their low absorption cross-sections at wavelengths greater than 180 nm. Examples of these are methane, ethane, and water (all of which are known to exist in the jovian atmosphere), which have very low absorption cross-sections beyond 140, 160, and 175 nm, respectively. (Water indigenous to Jupiter is expected to be condensed at pressures greater than 5 bar; small amounts could, however, enter Jupiter's upper atmosphere as a result of meteorite/comet ablation.) Other absorbers which might contribute to the absorption of solar photons are hydrazine, methylamine, and hydrogen sulfide. Hydrazine, N_2H_4, which has a low vapor pressure at jovian temperatures, is thought to condense at these altitudes. The low abundance, along with a decreasing cross-section longward of 200 nm, is consistent with the absence of a signature in the reflectance spectra at these wavelengths. We include the photoabsorption of gaseous hydrazine in our photochemical model, since it is important in recycling ammonia (Atreya *et al.* 1977), but it does not play a role in determining the albedo. The optical constants of condensed hydrazine have not been measured at UV wavelengths below 280 nm, so it is not included as a possible candidate for aerosol absorption. Methylamine does not appear to show a signature in the reflectance spectra. We have included it in our photochemical model as a source of coupling between the nitrogen and hydrocarbon chemistries (Kuhn *et al.* 1977; Kaye and Strobel 1984) as CH_3 could react with the NH_2 radical and inhibit formation of ammonia. Hydrogen sulfide has an absorption continuum similar to phosphine but with a shift in the peak absorption to longer wavelengths. This similarity and the fact that there are no discrete spectral signatures in either the PH_3 or H_2S cross-sections in the wavelength region of interest makes it difficult to distinguish between the two unless they are present in large abundance. On the other hand, neither ground-based infrared data (Larsen *et al.* 1984) nor *in situ* measurements with the Galileo probe mass spectrometer (Niemann *et al.* 1996) indicate the presence of H_2S above the ammonia ice clouds. Consequently, H_2S is not included in our analysis. Many other candidates have been considered as possible absorbers with none showing strong evidence of a spectral signature.
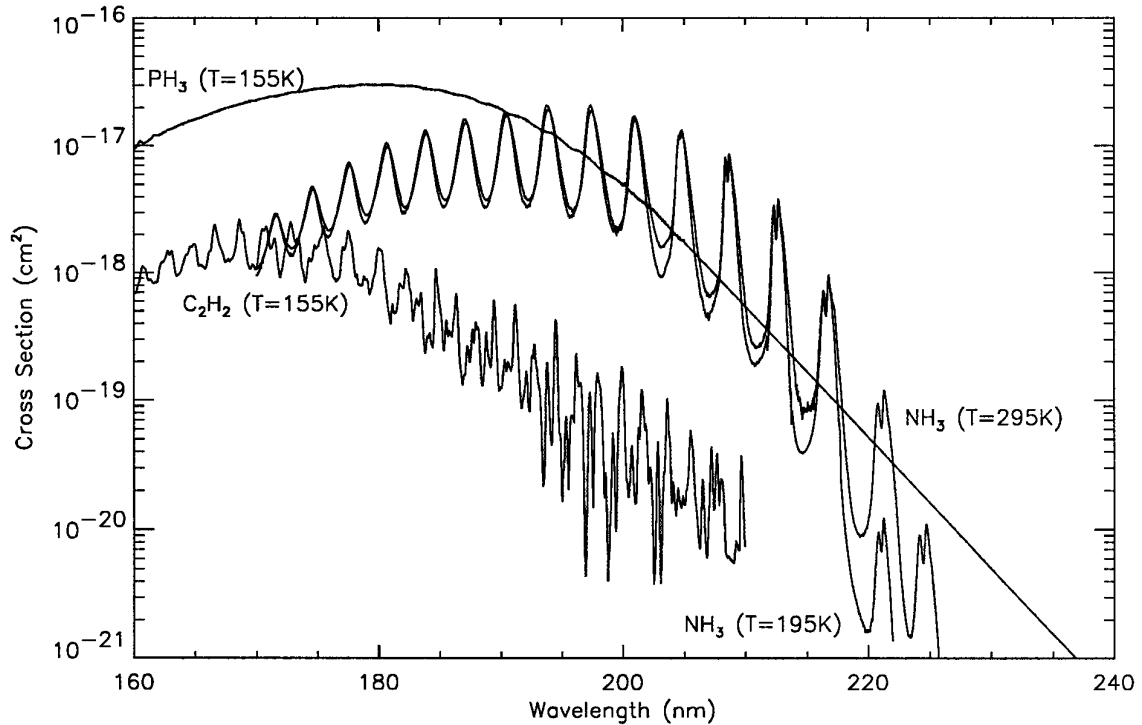
FIG. 3.   Cross sections of several chemical species that could tentatively contribute to the observed reflectance.

Ammonia absorption from 170 to 230 nm is due to the $\tilde{X}^1 A_1 \rightarrow \tilde{A}^1 A_2''$ transition. Several vibronic bands are present in this wavelength interval with peak absorption occurring around 190 nm. Even though the ammonia cross-section peaks around 190 nm, there is no signature of ammonia shortward of 200 nm in our observations (Fig. 2). Instead, in this region of the spectrum (<200 nm), acetylene has a fairly large cross-section and is abundant enough to show its spectral signature. Figure 4a shows the 6°N spectra and the model fits of several ammonia altitude profiles considering only the effect of ammonia absorption on the albedo. The altitude profiles include a homogeneous (constant ammonia mixing ratio of 1.0×10^{-8}) profile (dotted curve) and one generated with the use of our photochemical model that provides the best fit to the reflectance spectra in the wavelength interval 200–220 nm (dashed curve). On the basis of the constant mixing ratio profile, one would expect to observe peak ammonia absorption near 195 nm. Comparison with the spectra shows that this is not the case, requiring a case where the ammonia varies with altitude. The preferred fit is the one given by our photochemical model, which shows ammonia absorption in the spectral region where a signature is observed in the FOS data. A similar result was obtained by Visconti (1981).

The divergence of the synthetic fits from observation at short wavelengths is due to less ammonia being present near the level of unit scattering optical depth. At short

wavelengths (<180 nm), the light is Rayleigh scattered from higher altitudes (<100 mbars) as a consequence of the larger scattering cross-section. A small amount of ammonia is present in this pressure region due to photolysis. The low abundance of ammonia results in the lack of a signature for ammonia. At longer wavelengths (220 nm), the light can penetrate to levels >100 mbars, where there is a substantial amount of ammonia that can absorb photons. As a result, we see a signature of ammonia which has its peak absorption near 210 nm. Beyond 220 nm, laboratory measurements at room temperature give NH_3 absorption cross-section decreasing with increasing wavelength. At the low temperatures that exist on Jupiter, the bands at longer wavelengths are even weaker than the corresponding room-temperature cross sections (Chen *et al.* 1995), which agrees with the nondetection of the band near 228 nm in the reflectance spectrum. Figure 4b shows the effect of using room temperature cross-sections with the "best fit" ammonia profile from the low temperature case on the synthetic spectrum (dotted curve). Use of the room-temperature cross-sections would produce at least one more absorption peak at 221 nm that would result in more absorption than is actually needed to fit the data; no absorption feature is apparent at this wavelength. In both the low- and room-temperature cases at wavelengths greater than 210 nm, the albedos of our model fits diverge from the actual observed spectrum. The minima in the
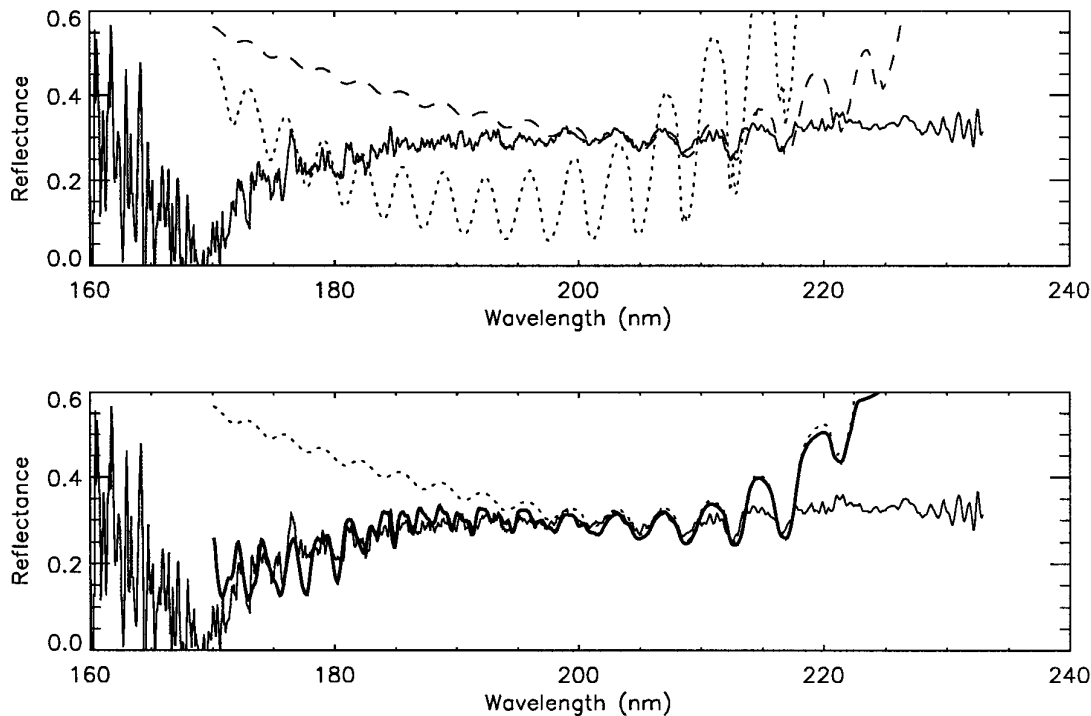
FIG. 4. (a) 6°N normal reflectance (solid line); synthetic spectrum assuming a constant mixing ratio of 1.0×10^{-8} for ammonia (dotted); synthetic spectra using photochemically generated ammonia assuming room temperature cross sections for ammonia (dashed). (b) 6°N normal reflectance (solid line); synthetic spectrum assuming low temperature cross sections for ammonia (dotted); synthetic spectrum using low temperature cross section for ammonia along with acetylene (bold).

ammonia cross-sections do not provide enough absorption to match the continuum level. In order to account for the absorption at longer wavelengths and at the minima of the ammonia cross-sections, modeling of aerosol particles or some other continuum absorber, to be discussed later, needs to be invoked.

Acetylene absorption takes place below 200 nm (Chen *et al.* 1991). The origin of the bands above 185 nm is attributed to the $\tilde{X}^1\Sigma_g^+ \rightarrow \tilde{A}^1A_u$ transition and those below transition and those below 185 nm to the $\tilde{X}^1\Sigma_g^+ \rightarrow \tilde{B}^1B_u$ system. The identification of acetylene can be seen by comparing the structure in its cross-section with the observations (Figs. 2 and 3). To determine the abundances of acetylene, we have tried several distributions of both ammonia and acetylene obtained by varying the eddy diffusion profiles in our photochemical model. Our best fit with acetylene is shown in Fig. 4b (bold curve). As seen in the fits with ammonia only, the ammonia would provide the bulk of the opacity in this wavelength region, if photons were allowed to penetrate to greater depths, where the ammonia is present. Since the Rayleigh scattering is unity above this for wavelengths less than 185 nm, too many photons would be scattered out of the atmosphere. Even though photochemical models of the jovian atmosphere show that acetylene is formed at higher altitudes (μbar

region) with larger mixing ratios than in the lower stratosphere, the optical depth of absorbing and scattering material, i.e., acetylene plus hydrogen, does not reach unity until approximately the 50 mbar region for the wavelength interval of interest. The low albedo and the strong acetylene signature observed in our spectrum along with the results of the photochemical model imply that we are observing acetylene in a region of the atmosphere above the level where ammonia is being photolyzed. The acetylene abundance calculated by our photochemical models is fairly constant, with mixing ratios of about $(10–30) \times 10^{-9}$ throughout the altitude region that we are sampling. Yet as shown in Fig. 4b, the photochemical distribution of acetylene does not provide a perfect fit to our data in the 180- to 200-nm region, which is already uncertain due to grating scattered light. The contrast in the acetylene absorption bands, defined here as the depth of a feature with respect to the continuum, is smaller than the bands in the synthetic spectrum. Adding more acetylene would decrease the continuum at the expense of increasing the contrast. A small amount of aerosol material or some other continuum absorber near altitudes where acetylene absorbs, on the other hand, would decrease the simulated albedo and also reduce the contrast. This could have a small effect on the ammonia distribution needed to fit the spectra, depending upon the

spectral properties of this haze and its optical depth, since the radiation budget of the atmosphere is modified. It should be stressed that the absolute calibration of the intensity is unknown shortward of 180 nm, since the grating-scattered light becomes increasingly important at these wavelengths. Hence, we do not attempt to model this haze layer.

Phosphine absorption in the 180- to 230-nm spectral region is due to the $\tilde{X}^1A_1 \rightarrow \tilde{A}$ transition and is a continuum with a maximum near 180 nm. An unambiguous identification of phosphine is not possible, since no band structure is present in its absorption cross-section and no broad minimum can be seen in the I/F spectra. Even if phosphine were present, its absorption properties could be mimicked by aerosols or other species with a broad absorption continuum (Fig. 6). The photochemical profile of phosphine shows that PH$_3$ is expected to be confined to deeper levels of the atmosphere, i.e. below the region of ammonia photolysis. This is the result of phosphine having a lower mixing ratio than ammonia near 1 bar (6×10^{-7}, Kunde *et al.* 1982). The larger optical depth of ammonia compared to phosphine results in ammonia completely dominating the albedo and phosphine being undetectable. Similar results are obtained for 15°N, 20°N, and 25°N.

In order to test if possible larger phosphine abundances are tolerable, we have run several cases where phosphine is assumed to have a uniform mixing ratio below a certain altitude and zero above. If phosphine is constrained to lie below 30 km (250 mbar), we need an amount that is larger than solar by about a factor of 50 (solar P/H = 3.73×10^{-7}; Anders and Grevesse 1989). We find this abundance unrealistic considering the strong possibility that aerosols could provide the required opacity. This amount of phosphine has a negligible impact on the spectral region dominated by ammonia absorption but has a large impact on the continuum level beyond 225 nm as Rayleigh scattering allows photons to penetrate below 30 km. If the phosphine is required to be uniformly mixed below 50 km, a mixing ratio larger than 2×10^{-9} tends to dominate the albedo from 190 to 210 nm. Longward of 210 nm, the albedo is too large as the phosphine cross-section, hence the absorption optical depth, decreases at longer wavelengths. If the phosphine is constrained to exist below 40 km, we can tolerate an upper limit of 1.5×10^{-7} for the phosphine mixing ratio beyond which it would dominate the synthetic reflectance spectra. If we allow phosphine to vary with altitude, the following dependence of mixing ratio, ξ_{PH_3} vs pressure provides a good fit to the observations at 6°N,

$$\xi_{PH_2} = \begin{cases} 6 \times 10^{-7} \left(\dfrac{p}{1000} \right)^{0.1}, & p > 200 \text{ mbar} \\[2em] 5.1 \times 10^{-7} \left(\dfrac{p}{200} \right)^{10}, & p < 200 \text{ mbar} \end{cases} \quad (9)$$

where p is in mbar. This parameterization gives sufficient absorption to fit the continuum to about 225 nm. To fit the spectrum at wavelengths greater than 225 nm requires abundances larger than solar at pressures greater than 200 mbar. This is different from the altitude profile produced by the photochemical model in which phosphine is photolyzed deeper in the atmosphere. Clearly more laboratory work on the chemical kinetics of phosphorus compounds in hydrogen atmospheres needs to be conducted so that the photochemistry can be correctly evaluated.

As seen above, for low latitudes, aerosols are a possibility for reproducing the continuum level at wavelengths longer than 220 nm and at the minima of the ammonia absorption cross-section bands (Fig. 3), as ammonia alone does not account for the observed reflectivities. Aerosols could also contribute to the opacity at wavelengths where acetylene absorbs, as shown above. Many factors involved in modeling aerosols in the atmosphere, including the composition of the aerosol particles, are unknown, leading to many possible combinations of size distribution, number density, and indices of refraction that can give similar results. There are few constraints on the composition, size distribution, and altitude level of the haze particles as derived from the data presented here. These uncertainties, combined with a lack of appropriate laboratory optical constant measurements, results in unconstrained scattering properties of the atmosphere, whereas with a pure Rayleigh–Raman scattering atmosphere, the scattering properties of the atmosphere are constrained by the choice of model atmosphere (temperature and pressure as a function of altitude). Due to uncertainties in constraining the aerosol parameters and the dominance of gaseous absorption at low latitudes, we have tried to minimize the impact of the aerosol on the portion of the spectrum where ammonia absorption is dominant. Here we are only interested in modeling the continuum longward of the ammonia absorption bands up to 230 nm. The analysis of data at longer wavelengths will be discussed in a later publication; in this paper, we are concerned with gaseous absorption which dominates the spectrum below 230 nm. We have modeled the aerosols using spheres with a mean radius of 0.3 μm and an index of refraction of 1.4–i0.3, where Mie scattering theory was used to determine the optical properties of the aerosol particles.

As with phosphine, the altitude distribution and abundance of the aerosol particles were adjusted until a reasonable fit to the continuum at long wavelengths was obtained. For the low latitudes, we assume the "mixing ratio" of the aerosol particles to be uniformly mixed with altitude below the 100-mbar level, the region where ammonia is being photolyzed. The aerosol mixing ratio needed for the best fits to the spectrum is 3.0×10^{-18}. This corresponds to a total optical depth of 2.1 between 100-1000 mbar at 220 nm. We find that the absorption properties, i.e., the single
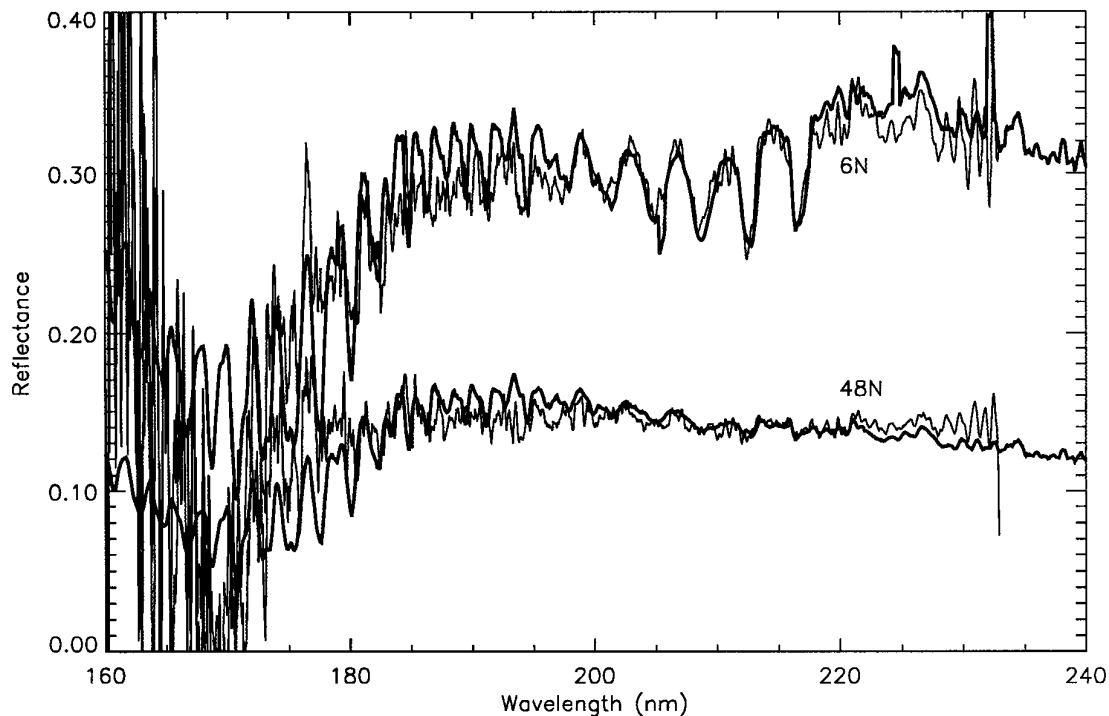
FIG. 5. Fits to 6°N and 48°N spectra including ammonia, acetylene, phosphine, and haze as sources of opacity. Synthetic spectra similar to 6°N were also fitted to the other low latitude (15°N, 20°N, and 25°N) spectra. These are not shown as they exhibit similar features and continuum levels.

scattering albedo and phase function, of the aerosol material vary with wavelength so that both the observed ammonia bands and the continuum at wavelengths longer than 220 nm are reasonably simulated.

We have also considered the scenario where the haze is made up of ammonia crystals which we treat as Mie particles and use the refractive indices given in Martonchik *et al.* (1984). The haze was constrained to exist in the region where gaseous ammonia condenses to ammonia ice. Inclusion of condensed ammonia in this manner gives a poor fit for any aerosol density distribution. In the 200- to 230-nm region, the imaginary refractive index of ammonia is too low, making the crystals too reflective to provide a fit to the albedo. Hence, the synthetic albedo remains too large at these wavelengths. Variation of the mean size of the particles does not change this result. This could imply the existence of a contaminant which increases the absorption properties of the ammonia crystals at these wavelengths or the presence of another type of aerosol in agreement with the findings of Tomasko *et al.* (1978). Several candidate materials for these aerosols are solid hydrocarbons, tholins (e.g., Khare *et al.* 1987), and solid hydrazine, for which optical constants in the UV have not been published.

In Fig. 5, we show a fit to the 6°N spectra including the effects of ammonia, acetylene, phosphine, and haze. From 6°N to 25°N, the albedo decreases slightly with increasing latitude. Hence, we do not show fits to spectra at other latitudes. Most of the change in albedo for the 15°N, 20°N, and 25°N spectra relative to 6°N can be attributed to the variation in the solar zenith and the Earth viewing angles for the observations. This is due to longer geometrical path lengths for the photons resulting in an increased likelihood of their absorption or Rayleigh scattering. Only slight changes in the eddy diffusion coefficient, which changes the ammonia distribution, are required to provide better fits to the FOS reflectivities. Comparison of the mixing ratio profiles of ammonia and vertical eddy mixing for 6°N to 25°N reveals that very little change with latitude is present with a trend of less mixing and less ammonia required with increasing latitude. Figures 6 and 7 show altitude profiles and eddy diffusivities derived from the FOS spectra for 6°N–25°N.

The photochemical models that assume a Rayleigh scattering atmosphere with minimal aerosols break down in interpreting the observations at higher latitudes (48°N, 65°N) and of the equatorial plume spectra, since we observe an albedo which is nearly gray with wavelength (Fig. 2). If Rayleigh scattering was dominant in the presence of a gray absorber, one would expect to see a variation with wavelength as observed in the lower latitude spectra (Fig. 2). In addition, the albedos are lower compared to those
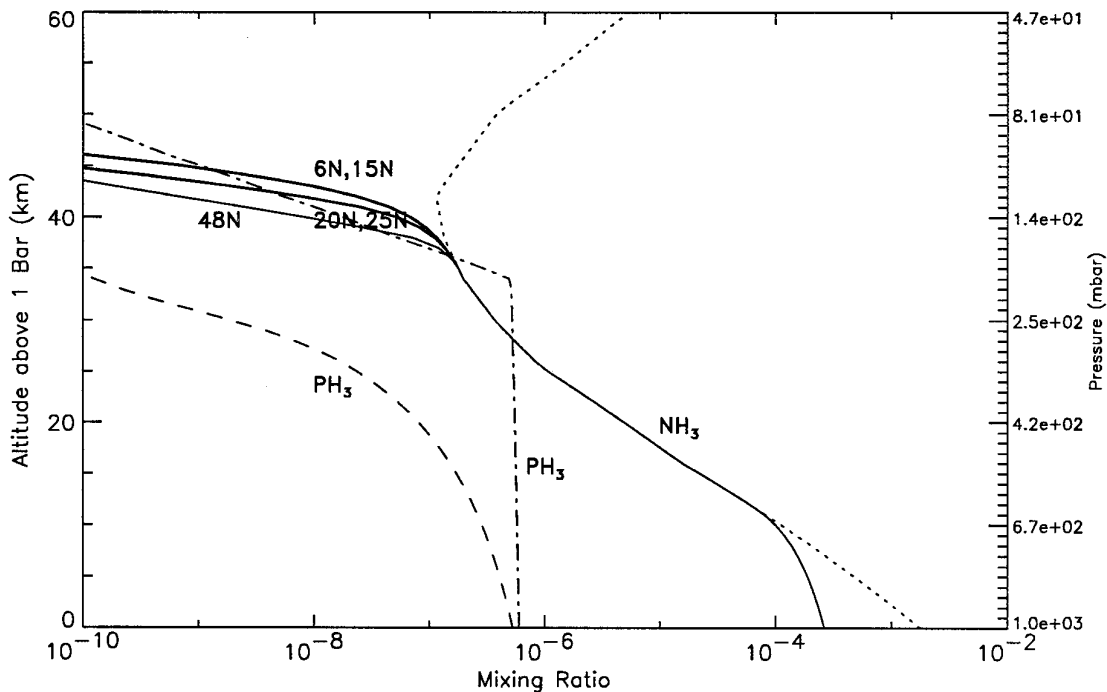
FIG. 6. Mixing ratio versus altitude for key species considered in this analysis. Several latitudes are plotted: 6°N, 15°N, 20°N, 25°N, and 48°N (solid line). The profiles for 6°N and 15°N nearly overlay each other with the same being true of 20°N and 25°N. We also show the photochemical distribution of phosphine at 6°N (---), the best fit for phosphine at 6°N (dot-dashed), and the saturated ammonia profile (···). Note that below the 600-mbar pressure level, ammonia is sub-saturated. This lower boundary does not affect the photochemical distribution above this level as condensation becomes an important constraint. The modeled reflectivity is also unaffected since Rayleigh scattering by the atmosphere and scattering by cloud particles prevents photons from reaching below the ammonia clouds.

at low latitudes. This cannot be accounted for on the basis of geometry alone, indicating that aerosol material dominates the scattering properties of the atmosphere. This aerosol would have to lie above the Rayleigh scattering atmosphere. For the high latitudes, the darkening is produced by the enhanced absorption of photons relative to scattering caused by longer geometric path lengths through some unknown species/aerosol located higher in the atmosphere such that fewer photons are scattered back by Rayleigh scattering. Thus the albedo is less than that of the clearer Rayleigh scattering atmosphere at lower latitudes. This aerosol layer is consistent with previous observations by Voyager and other ground-based instruments, which indicate that a polar haze exists at high latitudes (West *et al.* 1986; West 1988). The equatorial plume also is darker because of the presence of a more strongly UV-absorbing material and the small zenith angle at which the spectrum was taken.

Haze parameters that would be consistent with the continuum of the 48°N spectrum shown in Fig. 2 are an index of refraction of 1.4–i0.3, a size of 0.003 μm, and a uniform distribution with mixing ratio 1.2×10^{-12} below the 0.1 mbar level. The optical depth at 220 nm between 0.1 and 1000 mbar is 2.19. Although this optical depth is nearly

the same as that at 6°N, the aerosol particles are more absorbing and are distributed to higher altitudes, thus leading to a smaller albedo at 48°N. The small size leads to less of a wavelength variation than would a large particle size. Large particle sizes along with a varying index of refraction could accomplish the same fit to the albedo.

Two FOS spectra were taken for each of 48°N and 65°N. Comparing the spectral pairs for each latitude, we found large differences in the albedo. These differences could be due to pointing uncertainty as these spectra were taken nearer the limb and are more sensitive to the exact geometry of the observations. This could also indicate the existence of longitudinal inhomogeneities at high latitudes. By way of contrast, two spectra taken at 6°N show very little difference in absolute albedo, suggesting that ammonia and other absorbing species are well mixed zonally. The behavior observed at 6°N might be expected given the long lifetimes of ammonia and acetylene in the jovian atmosphere (~0.1 and ~3 yr, respectively). Inhomogeneities at the high latitudes might be caused by the highly variable nature of the jovian aurora. Ionization by energetic particles in the polar regions would promote the destruction of methane and the creation of heavier hydrocarbons that could condense to form aerosols (Pryor and Hord, 1991).
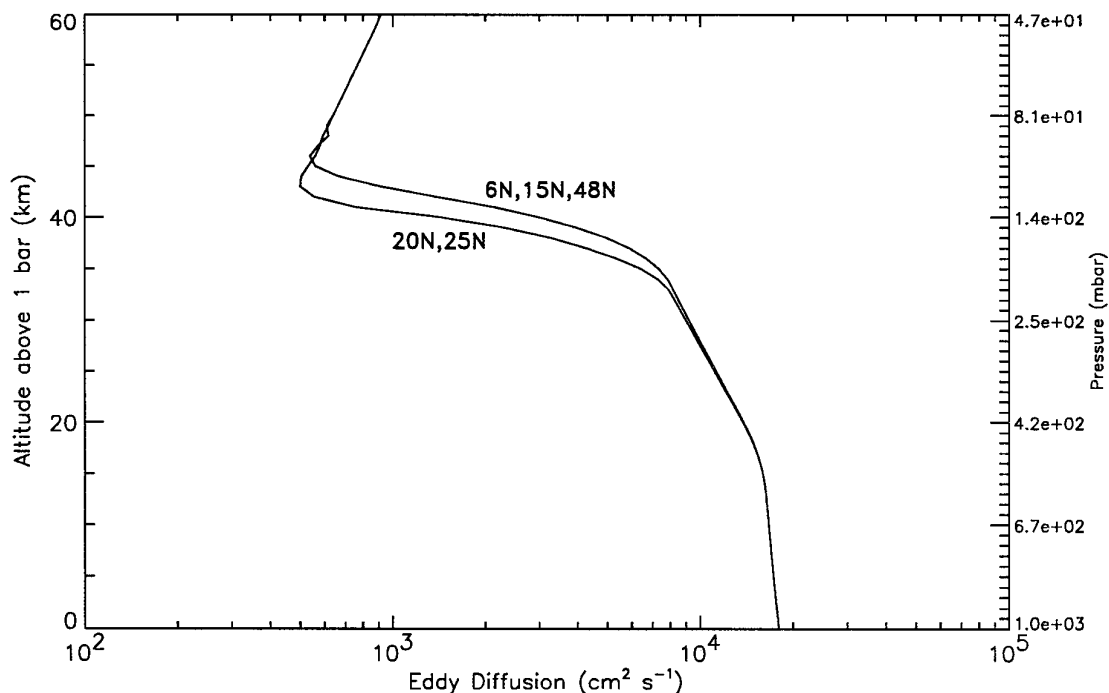
FIG. 7. Eddy diffusivity as a function of altitude for latitudes 6°N, 15°N, 20°N, 25°N, and 48°N. The same eddy diffusion coefficients are needed for 6°N, 15°N, and 48°N, and for 20°N and 25°N.

In the 48°N and equatorial plume spectra, weak ammonia and acetylene signatures can still be seen in the spectra (Fig. 2). As these absorption signatures are clearly weaker than those at lower latitudes, a smaller abundance of these species is observed due to the presence of the aerosols in the region. Figure 6 also shows the ammonia distribution that is needed along with the above aerosol parameters in order to reproduce the 48°N spectrum shown in Fig. 5. As the aerosol parameters providing a source of opacity are uncertain, the ammonia profile is also likely to be uncertain. Hazes at 65°N obscure the presence of any ammonia or phosphine that may be present in the atmosphere at those latitudes.

DISCUSSION AND CONCLUSIONS

The derived altitude profiles of ammonia are valid primarily in the region of the atmosphere where the slant optical depth is approximately unity, since in a statistical sense, most of the reflected light originates from this level. Owing to photolysis, one finds that peak absorption due to ammonia takes place around 40–45 km above the 1-bar level, that is, in the 100- to 200-mbar region near the point where the ammonia abundance departs from saturation. Acetylene absorption dominates above this level, proven by the lack of an ammonia signature at wavelengths less than 190 nm and a reduced albedo compared to the "Ray-

leigh scattering plus ammonia" case (Fig. 4b). Throughout most of and below the ammonia condensation region, the observations are insensitive to the abundance of ammonia since the optical depth increases rapidly with depth so that the solar photons cannot penetrate to these levels. Figure 6 compares the vertical mixing ratio of ammonia at 6°N, 15°N, 20°N, and 25°N. Most of the variation seen in the low latitude spectra is thus attributed to the geometry of observations. We find that only slight changes in the vertical profiles of ammonia are needed at low latitudes to reproduce the reflectivities. As latitude increases, less ammonia is needed at a given pressure level.

The value of the eddy diffusion coefficient at 6°N deviates from the power law given in Eq. (8) near 80 mbar. Stronger mixing is needed to increase the ammonia mixing ratio so that a fit to the FOS data can be obtained. The required eddy profile is shown in Fig. 7. A rapid increase in value from 5 $\times 10^2$ cm^2 s^{-1} to 10^4 cm^2 s^{-1} is needed from 90 to 150 mbar. This is followed by a less rapid increase to 1.5×10^4 cm^2 s^{-1} at 500 mbar. We are most sensitive to the value between 80 and 150 mbar, since the ammonia signature in our spectra originates from these pressure levels.

Similar to the ammonia profiles, the eddy mixing profile is found not to vary much over low latitudes (Fig. 7). We find that only slightly different eddy profiles are needed to produce the ammonia altitude profiles shown in Fig. 6, with a "trend" that less vertical mixing is needed as the

latitude is increased to 25°N. For the aerosol parameters chosen for modeling the 48°N reflectivities, an eddy mixing profile similar to that of 6°N can provide the ammonia mixing ratios necessary for a fit. Choosing different aerosol parameters will require modification of the eddy profile as the opacity and hence the required ammonia distribution changes. For this reason, 48°N results are uncertain.

The derivation of a tropospheric eddy diffusion coefficient in this paper depends on the authenticity of the photochemical models used, particularly the one for ammonia and phosphine. The model, by the same token, relies on the availability of good laboratory chemical kinetics data for the relevant reaction pathways. For example, Prasad and Capone (1976) have shown that use of a slower rate than that of Gordon *et al.* (1971) for the reaction $NH_2 + NH_2 + M \rightarrow N_2H_4 + M$ changes the ammonia distribution for a given eddy mixing profile. We have confirmed with our model that such sensitivity exists. As the ammonia distribution required to fit the FOS reflectivities would remain unchanged, changes in the eddy diffusion coefficients would be necessary to refit the observations if the rates of major reaction pathways were measured to be significantly different.

Acetylene abundances can be estimated from our spectra, but due to grating-scattered light, the quality of the FOS spectra degrades shortward of 185 nm. The continuum becomes highly dependent upon the choice of correction for the grating scatter, a problem that next generation spectrographs, such as the Space Telescope Imaging Spectrograph, should be able to overcome. Thus we are sensitive to only a small portion of the acetylene absorption cross section, which decreases rapidly with increasing wavelength. This, combined with uncertainties of 20–30% in laboratory measurements of acetylene cross-sections (Wu *et al.* 1989; Smith *et al.* 1991), make it difficult to determine the acetylene abundances and altitude information with greater accuracy. Our estimated abundances are in agreement with previous observations by IUE and sounding rockets (Wagener *et al.* 1985; Owen *et al.* 1980; Giles *et al.* 1976).

At best, only upper limits can be determined for the abundance of phosphine. This is a strong function of the pressure level where phosphine is placed. A possible altitude profile has been derived for phosphine (Eq. 9). The photochemical profile, on the other hand, shows that phosphine is only present at deeper levels, so that it is obscured by ammonia and any overlying haze. Lack of detailed chemical kinetics information makes the photochemical profile questionable, although it is in closer agreement with the Voyager IRIS profile (Kunde *et al.* 1982; Carlson *et al.* 1994). While phosphine is a possible candidate for providing continuum absorption, large abundances are needed to provide the necessary absorption beyond 225 nm.

Aerosols are a strong candidate for providing the neces-

sary continuum absorption through the entire spectral region covered by the FOS. For low latitudes, haze parameters can be chosen such that there is a negligible effect upon the portion of the spectrum dominated by ammonia absorption. The spectra taken with the FOS at high latitudes and of the equatorial plume reveal little or no information about the altitude distribution of ammonia, phosphine, and acetylene as these spectra are dominated by the opacity of aerosol particles which obscure any molecular species that could be present in the atmosphere. As the composition of the aerosol material is uncertain and laboratory measurements of optical constants are scant for but a few molecules, information about the size and distribution of aerosol particles with altitude is nonunique. Analysis of G270H spectra may better characterize the aerosol parameters.

APPENDIX: GEOMETRY OF OBSERVATIONS

For each observation, it is important for the radiative transfer calculations that need to be performed in simulating the albedo spectrum to account properly for the directions of the Earth and the Sun relative to the observed location on the planet, because (1) Rayleigh scattering by molecular hydrogen and helium is anisotropic, and (2) the pathlength is highly dependent upon the Sun/Earth positions relative to the point of observation. The longitude and latitude of the subsolar and sub-Earth points of Jupiter were determined from published ephemerides (*The Astrophysical Almanac* 1992) for the times of observation. Letting the latitude and longitude of an observation be represented by θ_0 and ϕ_0, respectively, the local solar and Earth zenith angles can be determined from the formula

$$\cos\Theta = \frac{(\mathbf{r} - \mathbf{r}_0) \cdot \mathbf{r}_0}{|\mathbf{r} - \mathbf{r}_0||\mathbf{r}_0|}$$

$$= \frac{rr_0\sin\theta\sin\theta_0\cos(\phi - \phi_0) + rr_0\cos\theta\cos\theta_0 - r_0^2}{r_0[r^2 + r_0^2 - 2rr_0\sin\theta\sin\theta_0\cos(\phi - \phi_0) - 2rr_0\cos\theta\cos\theta_0]^{0.5}}$$

(12)

where $\mathbf{r}$ and $\mathbf{r}_0$ are the vectors from the center of Jupiter to the Sun/Earth and to the point of observation, respectively. This can be greatly simplified by assuming that $|\mathbf{r}| \gg |\mathbf{r}_0|$. In this case the equation describing the zenith angle becomes

$$\cos\Theta = \mu = \sin\theta\sin\theta_0\cos(\phi - \phi_0) + \cos\theta\cos\theta_0. \quad (11)$$

In calculating the diurnal average, it is useful to know the average solar zenith angle during the daylight hours. This is given by

$$\langle\mu\rangle = \int_{Dawn}^{Noon} [\sin\theta_S\sin\theta\cos(\phi_S(t) - \phi) + \cos\theta_S\cos\theta]\,dt \quad (12)$$

Performing the integration we obtain (Liou 1980; Romani and Atreya 1988)

$$\langle\mu\rangle = \frac{1}{h}\sin\theta_S\sin\theta\sin(h) + \cos\theta_S\cos\theta, \quad (13)$$

where h is the half-length (in radians) of the illuminated day. The following set of equations permits the calculation of the half-length.

$$\chi = -\cot(\theta_S)\cot(\theta)$$

$$h = \begin{cases} \cos^{-1}(\chi) & \\ 0, & \text{if } \chi \geq 1 \\ \pi, & \text{if } \chi \leq -1. \end{cases} \quad (14)$$

We assume the solar flux to originate from this average zenith angle during the daylight hours. We also neglect twilight effects and assume zero flux during the night time.

Since scattering processes are anisotropic, to accurately determine the intensity of a ray leaving the atmosphere, we need to calculate the difference in the azimuth angles. The azimuth angle between the Earth and Sun in the local horizontal plane is given by

$$\cos\Phi = \frac{[(\mathbf{r}_S - \mathbf{r}_0) - (\mathbf{r}_S - \mathbf{r}_0)\cdot\hat{\mathbf{r}}_0\hat{\mathbf{r}}_0]\cdot[(\mathbf{r}_E - \mathbf{r}_0) - (\mathbf{r}_E - \mathbf{r}_0)\cdot\hat{\mathbf{r}}_0\hat{\mathbf{r}}_0]}{|(\mathbf{r}_S - \mathbf{r}_0) - (\mathbf{r}_S - \mathbf{r}_0)\cdot\hat{\mathbf{r}}_0\hat{\mathbf{r}}_0||(\mathbf{r}_E - \mathbf{r}_0) - (\mathbf{r}_E - \mathbf{r}_0)\cdot\hat{\mathbf{r}}_0\hat{\mathbf{r}}_0|}, \quad (15)$$

where $\mathbf{r}_S$, $\mathbf{r}_E$, $\mathbf{r}_0$, and $\hat{\mathbf{r}}_0$ are the vectors from the center of Jupiter to the Sun, to the Earth, and to the point of observation, and the unit radial vector, respectively. This equation can be approximated by the following:

$$\cos\Phi = \frac{[\mathbf{r}_S - \mathbf{r}_S\cdot\hat{\mathbf{r}}_0\hat{\mathbf{r}}_0]\cdot[\mathbf{r}_E - \mathbf{r}_E\cdot\hat{\mathbf{r}}_0\hat{\mathbf{r}}_0]}{|\mathbf{r}_S - \mathbf{r}_S\cdot\hat{\mathbf{r}}_0\hat{\mathbf{r}}_0||\mathbf{r}_E - \mathbf{r}_E\cdot\hat{\mathbf{r}}_0\hat{\mathbf{r}}_0|}. \quad (16)$$

The calculated values of the above solar zenith, average solar zenith, Earth zenith, and azimuth angles are shown in Table II.

ACKNOWLEDGMENTS

REFERENCES

Allen, 1973. *Astrophysical Quantities*, 3rd ed. Athlone Press, London.

Anders, E., and N. Grevesse 1989. Abundances of the elements: Meteoritic and solar. *Geochim. Cosmochim. Acta* **53**, 197–214.

Atreya, S. K., and P. N. Romani 1985. Photochemistry and clouds of Jupiter, Saturn, and Uranus. In *Planetary Meteorology* (G. E. Hunt, Ed.), pp. 17–68. Cambridge, UK: Cambridge Univ. Press.

Atreya, S. K., T. M. Donahue, and M. C. Festou 1981. Jupiter: Structure and composition of the upper atmosphere. *Astrophys. J.* **247**, L43–L47.

Atreya, S. K., T. M. Donahue, and W. R. Kuhn 1977. The distribution of ammonia and its photochemical products on Jupiter. *Icarus* **31**, 348–355.

Atreya, S. K., S. G. Edgington, L. M. Trafton, J. J. Caldwell, K. S. Noll, and H. A Weaver 1995. Abundances of ammonia and carbon disulfide in the jovian stratosphere following the impact of Comet Shoemaker-Levy 9. *Geophys. Res. Lett.* **22**, 1625–1628.

Beer, R., and F. W. Taylor, 1979. Phosphine absorption in the 5 μm window of Jupiter. *Icarus* **40**, 189–192.

Bishop, J., P. N. Romani, and S. K. Atreya 1997. Voyager 2 ultraviolet spectrometer solar occultations at Neptune: Photochemical modeling of the 125–165 nm lightcurves. *Planet. Space Sci.*, in press.

Brault, J. W., and O. R. White 1971. The analysis and restoration of astronomical data via the fast Fourier transform. *Astron. Astrophys.* **13**, 169–189.

Carlson, B. E., A. A. Lacis, and W. B. Rossow 1994. Belt-zone variations in the jovian cloud structure. *J. Geophys. Res.* **99**, 14,623–14,659.

Chandrasekhar, S. 1960. *Radiative Transfer*. Dover, New York.

Chen, F., D. L. Judge, C. Y. R. Wu, J. J. Caldwell, H. P. White, and R. Wagener 1991. High-resolution, low temperature photoabsorption cross sections of C_2H_2, PH_3, AsH_3, and GeH_4, with applications to Saturn's atmosphere. *J. Geophys. Res.* **96**, 17519–17527.

Chen, F., D. L. Judge, C. Y. R. Wu, and J. J. Caldwell 1997. Low- and room-temperature photoabsorption cross sections of NH_3 in the UV region. *J. Geophys. Res.*, submitted.

Clarke, J. T., H. W. Moos, and P. D. Feldman 1982. The far-ultraviolet spectra and geometric albedos of Jupiter and Saturn. *Astrophys. J.* **255**, 806–818.

Combes, M., R. Courtin, J. Caldwell, T. Encrenaz, K. H. Fricke, V. Moore, T. Owen, and P. S. Butterworth 1981. Vertical distribution of NH_3 in the upper jovian atmosphere from IUE observations. *Adv. Space Res.* **1**, 169–175.

Cochran, W. D., and L. M. Trafton 1978. Raman scattering in the atmospheres of the major planets. *Astrophys. J.* **219**, 756–762.

Cunningham, C. C., and J. J. Caldwell 1993. Grating scatter in the HST Faint Object Spectrograph. In *Calibrating the Hubble Space Telescope* (J. C. Blades and S. J. Osmer, Eds.), pp. 199–208. Space Telescope Science Institute, Baltimore.

dePater, I., and S. T. Massie 1985. Models of the millimeter–centimeter spectra of the giant planets. *Icarus* **62**, 143–171.

Fahr, A., A. Laufer, R. Klein, and W. Braun 1991. Reaction rate of determinations of vinyl radical reactions with vinyl, methyl, and hydrogen atoms. *J. Phys. Chem.* **95**, 3218–3224.

Fahr, A., P. S. Monks, L. J. Stief, and H. A. Laufer 1995. Experimental determination of the rate constant for the reaction of C_2H_3 with H_2 and implications for the partitioning of hydrocarbons in atmospheres of the outer planets. *Icarus* **116**, 415–422.

Festou, M. C., S. K. Atreya, T. M. Donahue, B. R. Sandel, D. E. Shemansky, and A. L. Broadfoot 1981. Composition and thermal profile of the jovian atmosphere determined by the Voyager ultraviolet stellar occultation experiment. *J. Geophys. Res.* **86,**, 5715–5725.

Ford, A. L., and J. C. Browne 1973. Rayleigh scattering cross sections for the hydrogen molecule. *Atomic Data* **5**, 305–313.

Giles, J. W., H. W. Moos, and W. R. McKinney 1976. The far ultraviolet (1200–1900 Å) spectrum of Jupiter obtained with a rocket-borne multi-channel spectrometer. *J. Geophys. Res.* **81**, 5797–5806.

Gladstone, G. R., M. Allen, and Y. L. Yung 1996. Hydrocarbon photochemistry in the upper atmosphere of Jupiter. *Icarus* **119**, 1–52.

Gordon, S., W. Mulac, and P. Nangia 1971. Pulse radiolysis of ammonia gas. II. Rate of disappearance of the $NH_2(X^2B_1)$ radical. *J. Phys. Chem.* **75**, 2087–2093.

Greenspan, J., and T. Owen 1967. Jupiter's atmosphere: Its structure and composition. *Science* **156**, 1489–1494.

Hanel, R., B. Conrath, M. Flasar, V. Kunde, P. Lowman, W. Maguire, J. Pearl, J. Perraglia, R. Samuelson, D. Gautier, P. Gierasch, S. Kumar, and C. Ponnamperuma 1979. Infrared observations of the jovian system form Voyager 1. *Science* **204**, 972–976.

Kaminski, J. W., and J. C. McConnell 1991. A note on the enhancement of J values in optically thick scattering atmospheres. *Can. J. Phys.* **69**, 1166–1174.

Kaye, J. A., and D. F. Strobel 1984. Phosphine photochemistry in the atmosphere of Saturn. *Icarus* **59**, 314–335.

Khare, B. N., C. Sagan, W. R. Thompson, E. T. Arakawa, and P. Votaw 1987. Solid hydrocarbon aerosols produced in simulated uranian and neptunian stratospheres. *J. Geophys. Res.* **92**, 1987.

Khe, P. V., J. C. Soulignac, and R. Lesclaux 1977. Pressure and tempera-

ture dependence of NH$_2$ recombination rate constant. *J. Phys. Chem.* **81,** 211–214.

Kuhn, W. R., S. K. Atreya, and S. Chang 1977. The distribution of methylamine in the jovian atmosphere. *Geophys. Res. Lett.* **4,** 203–206.

Kunde, V., R. Hanel, W. Maguire, D. Gautier, J. P. Baluteau, A. Marten, A. Chedin, N. Husson, and N. Scott 1982. The tropospheric gas composition of Jupiter's North Equatorial Belt (NH$_3$, PH$_3$, CH$_3$D, GeH$_4$, H$_2$O) and the jovian D/H ratio. *Astrophys. J.* **263,** 443–467.

Larsen, H. P., R. R. Treffers, and U. Fink 1977. Phosphine in Jupiter's atmosphere: The evidence from high altitude observations at 5 microns. *Astrophys. J.* **211,** 972–979.

Larsen, H. P., D. S. Davis, R. Hofmann, G. L. Bjoraker 1984. The jovian atmospheric window at 2.7 μm: A search for H$_2$S. *Icarus* **60,** 621–639.

Lindal, G. F., G. E. Wood, G. S. Levy, J. D. Anderson, D. N. Sweetnam, H. B. Hotz, B. J. Buckles, D. P. Holmes, P. E. Doms, V. R. Eshleman, G. L. Tyler, and T. A. Croft 1981. The atmosphere of Jupiter: An analysis of the Voyager radio occultation measurements. *J. Geophys. Res.* **86,** 8721–8727.

Liou, K.-N. 1980. *An Introduction to Atmospheric Radiation*. Academic Press, New York.

Martonchik, J. V., G. S. Orton, and J. F. Appleby 1984. Optical properties of NH$_3$ ice from the far infrared to the near ultraviolet. *Appl. Opt.* **23,** 541–547.

Monks, P. S., F. L. Nesbitt, W. A. Payne, M. Scanlon, and L. F. Stief 1995. Kinetics and products of the reactions between H and C$_2$H$_2$ at $T = 213$ K and $T = 398$ K. *J. Phys. Chem.* **99,** 17,151–17,159.

Mordaunt, D. H., I. R. Lambert, G. P. Morley, M. N. R. Ashfold, R. N. Dixon, C. M. Western, L. Schnieder, and K. H. Welge 1993. Primary product channels in the photodissociation of methane at 121.6 nm. *J. Chem. Phys.* **98,** 2054–2065.

Morrissey, P. F., P. D. Feldman, M. A. McGrath, B. C. Wolven, and H. W. Moos 1995. The ultraviolet reflectivity of Jupiter at 3.5 Å resolution from Astro-1 and Astro-2. *Astrophys. J.* **454,** L65–L68.

Niemann, H. B., S. K. Atreya, G. R. Carignan, T. M. Donahue, J. A. Haberman, D. N. Harpold, R. E. Hartle, D. M. Hunten, W. T. Kasprzak, P. R. Mahaffy, T. C. Owen, N. W. Spencer, and S. H. Way 1996. The Galileo Probe Mass Spectrometer: Composition of Jupiter's atmosphere. *Science* **272,** 846–849.

Noll, K. S., R. F. Knacke, A. T. Tokunaga, J. H. Lacy, S. Beck, and E. Serabyn 1986. The abundances of ethane and acetylene in the atmospheres of Jupiter and Saturn. *Icarus* **65,** 257–263.

Owen, T., J. Caldwell, A. R. Rivolo, V. Moore, A. L. Lane, C. Sagan, G. Hunt, and C. Ponnamperuma 1980. Observations of the spectrum of Jupiter from 1500 to 2000 Å with the IUE. *Astrophys. J.* **236,** L39–L42.

Particle Physics and Astronomy Research Council, 1995 *The Astronomical Almanac for the Year 1992*.

Prasad, S. S., and L. A. Capone 1976. The photochemistry of ammonia in the jovian atmosphere. *J. Geophys. Res.* **81,** 5596–5600.

Pryor, W. R., and C. W. Hord, 1991. A study of photopolarimeter system UV absorption data on Jupiter, Saturn, Uranus, and Neptune: Implications for auroral haze formation. *Icarus* **91,** 161–172.

Ridgway, S. T., H. P. Larsen, and U. Fink 1976. The infrared spectrum of Jupiter. In *Jupiter* (T. Gehrels, Ed.), pp. 384–417. Univ. Arizona Press, Tucson.

Romani, P. N. 1996. Recent rate constant and product measurements of the reaction C$_2$H$_3$ + H$_2$ and C$_2$H$_3$ + H—Importance for the photochemical modeling of hydrocarbons on Jupiter. *Icarus* **122,** 233–241.

Romani, P. N., and S. K. Atreya 1988. Methane photochemistry and haze production on Neptune. *Icarus* **74,** 424–445.

Seiff, A., D. B. Kirk, T. C. D. Knight, J. D. Mihalov, R. C. Blanchard, R. E. Young, G. Schubert, U. von Zahn, G. Lehmacher, F. S. Milos, and J. Wang 1996. Structure of the atmosphere of Jupiter: Galileo probe measurements. *Science* **272,** 844–845.

Smith, P. L., M. C. E. Huber, and W. H. Parkinson, 1976. Refractivities of H$_2$, He, O$_2$, CO, and Kr for $168 \leq \lambda \leq 288$ nm. *Phys. Rev. A* **13,** 1422–1434.

Smith, P. L., K. Yoshino, W. H. Parkinson, K. Ito, and G. Stark 1991. High-resolution, VUV (147–201 nm) photoabsorption cross sections for C$_2$H$_2$ at 195 and 295 K. *J. Geophys. Res.* **96,** 17,529–17,533.

Stamnes, K., S-C. Tsay, W. Wiscombe, and K. Jayaweera 1988. Numerically stable algorithm for discrete-ordinate-method radiative transfer in multiple scattering and emitting layered media. *Appl. Opt.* **27,** 2502–2509.

Strobel, D. F. 1973. The photochemistry of NH$_3$ in the jovian atmosphere. *J. Atmos. Sci.* **30,** 1205–1209.

Strobel, D. F. 1977. NH$_3$ and PH$_3$ photochemistry in the jovian atmosphere. *Astrophys. J.* **214,** L97–L99.

Tomasko, M. G. 1974. Ammonia absorption relevant to the atmosphere of Jupiter. II. Interpretation. *Astrophys. J.* **187,** 641–650.

Tomasko, M. G., R. A. West, and N. D. Castillo 1978. Photometry and polarimetry of Jupiter at large phase angles. I. Analysis of imaging data of a prominent belt and zone from Pioneer 10. *Icarus* **33,** 558–592.

Van Hoosier, M. E., J.-D. F. Bartoe, G. E. Brueckner, and D. K. Prinz 1988. Absolute solar spectral irradiance 120 nm–400 nm (results from the Solar Ultraviolet Spectral Irradiance Monitor–SUSIM—Experiment on board Spacelab 2). *Astron. Lett. Commun.* **27,** 163–168.

Visconti, G. 1981. Penetration of solar UV radiation and photodissociation in the jovian atmosphere. *Icarus* **45,** 638–652.

von Zahn, U., and D. M. Hunten 1996. The helium mass fraction in Jupiter's atmosphere. *Science* **272,** 849–851.

Wagener, R., J. Caldwell, T. Owen, S.-J. Kim, T. Encrenaz, and M. Combes 1985. The jovian stratosphere in the ultraviolet. *Icarus* **63,** 222–236.

Weisstein, E. W., and E. Serabyn 1994. Detection of the 267 GHz $J = 1$–0 rotational transition of PH$_3$ in Saturn with a new Fourier transform spectrometer. *Icarus* **109,** 367–381.

West, R. A. 1988. Voyager 2 imaging eclipse observations of the jovian high altitude haze. *Icarus* **75,** 381–398.

West, R. A., D. F. Strobel, and M. G. Tomasko 1986. Clouds, aerosols, and photochemistry in the jovian atmosphere. *Icarus* **65,** 161–217.

Wiscombe, W. 1977. The delta-M method: Rapid yet accurate radiative flux calculations for strongly asymmetric phase functions. *J. Atmos. Sci.* **36,** 1408–1422.

Wu, C. Y. R., T. S. Chen, G. S. Liu, D. L. Judge, J. J. Caldwell 1989. Photoabsorption of C$_2$H$_2$ in the 1530–1930 Å region: A temperature dependence study. *J. Chem. Phys.* **91,** 272–280.

Young, H. D. 1962. *Statistical Treatment of Experimental data: An Introduction to Statistical Methods*, McGraw–Hill, New York.